Influence of viscous layers on the growth of normal faults: insights from experimental and numerical models

Nicolas Bellahsen[a,b,*], Jean-Marc Daniel[a], Laurent Bollinger[c], Evgenii Burov[b]

[a]*Division Geologie–Geochimie, Institut Français du Pétrole, 1 et 4 avenue de Bois Preau, Rueil Malmaison 92852, France*
[b]*Université Pierre et Marie Curie, Paris 6, France*
[c]*LDG, CEA, Bruyères le Châtel, France*

Abstract

The influence in space and time of viscous layers on the deformation pattern of brittle layers is investigated using wet clay/silicone putty analogue models in extension. Brittle and brittle–viscous experiments at various extension velocities are compared. Numerical models are also performed to confirm the results and to control the boundary conditions. Our results show that: (i) the presence of a basal viscous layer localizes the deformation by creating faults with very large throw. This kind of deformation distribution constrains the location of small faults, with scattered orientations, in the vicinity of the larger, in particular in relay zones. (ii) A lower strength of the viscous layer (i.e. a low extension velocity) enhances this localization of the deformation. (iii) The displacement–length relationship and the spatial distribution of small-scale faults are strongly influenced by both the rheology of the model and the amount of extension. This study shows that they are important parameters, especially when characterizing the whole fault network evolution and the relationship between large and small faults. © 2003 Elsevier Science Ltd. All rights reserved.

Keywords: Normal faults; Analogue models; Numerical models; Viscous layers; Rheology; Displacement–length relationship

1. Introduction

Geometry, spacing and growth sequence are fault-network characteristics commonly explained in terms of both the rheology and the thickness of the brittle layer in which faults grow (Vendeville et al., 1987; Cowie and Scholz, 1992b; Cowie et al., 1993; Lavier et al., 1999; Ackermann et al., 2001). Using field studies, experimental and numerical models, a sequence of propagation for normal faults has been described as the combination of radial propagation (growth of an isolated fault by tip propagation) and segment linkage (Fig. 1) (Segal and Pollard, 1980; Peacock and Sanderson 1991; Cowie and Scholz, 1992b; Cowie et al., 1993; Cartwright et al., 1996; Marchal et al., 1998; Ackermann et al., 2001).

When the evolution of a complete fault network is described through statistical studies, two relationships are often computed: the displacement–length relationship and the size–frequency relationship. Both are characterized by power-law type functions (Watterson, 1986; Walsh and Watterson, 1988; Cowie and Scholz, 1992a; Dawers et al., 1993; Scholz et al., 1993; Clark and Cox, 1996; Nicol et al., 1996; Pickering et al., 1997; Cowie, 1998) and can be applied to estimate the strain contribution and the characteristics of small-scale faults. The following power-law relation expresses the displacement (D)–length (L) relationship:

$$D = cL^n \tag{1}$$

where c is the function of the mechanical characteristics of the layer, and n is the scaling exponent. Values for this exponent range from less than 1 (Fossen and Hesthammer, 1997; Gross et al., 1997; Ackermann and Schlische, 1999), to 1 (Cowie and Scholz, 1992a; Dawers et al., 1993; Schlische et al., 1996), 1.5 (Marrett and Allmendinger, 1991; Gillespie et al., 1992; Yielding et al., 1996) and, 2 (Watterson, 1986; Walsh and Watterson, 1988). Although most investigators agree that a value of 1 is a good rule, no consensus has yet been established about the value of n.

The presence of viscous layers and their strength are known to be important parameters controlling deformation

* Corresponding author. Current address: Dept. of Geological and Environmental Sciences, Stanford University, Stanford CA94305-2115, USA.

E-mail address: nicolasb@pangea.stanford.edu, nicolas.bellahsen@lgs.jussieu.fr (N. Bellahsen).
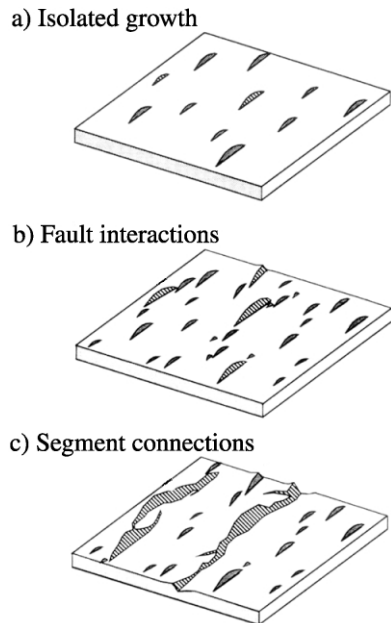
Fig. 1. Normal fault growth (from Cowie, 1998). (a) Isolated growth by tip propagation. (b) Interactions between fault segments. (c) Propagation by segment connection.

patterns. The importance of the mechanical layering has been demonstrated for the lithosphere (Allemand and Brun, 1991; Buck et al., 1999; Brun, 1999), the whole crust (Brun, 1999), and the upper brittle crust (Gross et al., 1997; Withjack and Callaway, 2000). The effects of brittle mechanical layering on fault network growth have been studied recently in an experimental work (Ackermann et al., 2001) and from field data (Schultz and Fossen, 2002). However, the effects of viscous layers have been under-studied, except in Davy et al. (1995) in a compressive context or in Withjack and Callaway, (2000) in basement-involved faulting.

In this paper, analogue and numerical models are used to demonstrate the influence of viscous layers on fault growth. For this purpose, fault networks generated with and without a basal viscous layer, and networks generated with a basal viscous layer under various extension velocities are compared. In each experiment, the general space-time evolution of normal fault networks is studied through three steps of extension, with particular attention paid to the spatial relationships between large and small faults.

2. Experimental procedure and dataset

2.1. Experimental set-up and materials

2.1.1. Boundary conditions

The experiments are performed in a deformation box (Fig. 2), with dimensions ranging between $60 \times 50 \times 10$ and $60 \times 70 \times 10$ cm. A basal rubber sheet fixed to rigid and movable walls induces nearly homogeneous extension in
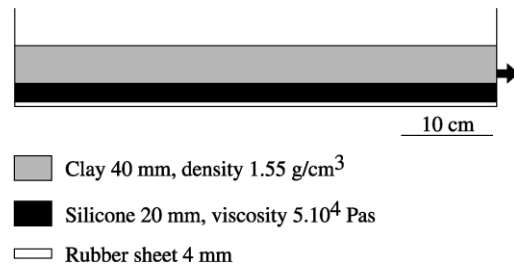

Fig. 2. Experimental set-up: the deformation box in cross-section. Two layers compose the model: one 4 cm thick layer of sand, one 2 cm thick layer of silicone. The two-layer model is underlain by a basal rubber sheet that applied the extension, whose velocity varied from 0.011 to 0.05 mm/s.

the overlying materials. The rubber sheet can be affected by strain gradients in the vicinity of the movable wall, especially at high extension rates and with a thick rubber sheet (Ackermann, 1997). This small departure from homogeneous extension affects the fault related strain but does not alter the results presented later in this paper. Fault networks are generated in a two-layer model, one 2 cm silicone lower layer and one 4 cm wet clay upper layer. Five experiments in a suite of 15 are used to demonstrate the influence of viscous layer on fault growth.

2.1.2. Analogue materials and scaling laws

The wet clay used here consists of a homogeneous mixture of water and pure industrial kaolinite powder. This kind of material has been previously used to simulate brittle behaviour (Cloos, 1968; Withjack and Jamison, 1986; Clifton et al., 2000; Withjack and Callaway, 2000; Ackermann et al., 2001). The water/kaolinite mixture in our experiments has a density of 1.55 g/cm³ (approximately 40% water). At the conditions and scale of the experiments, the wet clay behaves like a brittle material in which faults develop as illustrated in Fig. 3. The internal friction of the wet clay is about 0.5 (Sims, 1993). This value is similar to
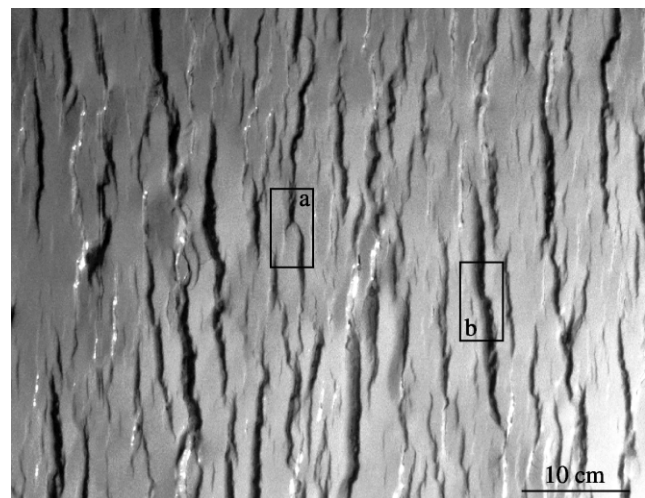

Fig. 3. Surface view of the fault network generated in wet clay. (a) Curvature of a fault segment and beginning of the coalescence. (b) Curvature of two segments leading to a single and undulating fault.

the internal friction of rocks in nature. The cohesion of the wet clay is estimated to 50 Pa (Sims, 1993). As inertial forces are neglected, the cohesion must satisfy the following dynamic similarity criterion:

$$C^* = \delta^* g^* \lambda^* \qquad (2)$$

where C^*, δ^*, g^*, and λ^* are the model-to-nature ratio for cohesion, density, gravity, and length, respectively (Hubbert, 1937). In our models, C^* is about 10^{-4}–10^{-5}, δ^* is about 0.6, and g^* is equal to 1. Thus, to ensure dynamic similarity and satisfy Eq. (2), the length ratio λ^* is about 1.5×10^{-4}–1.5×10^{-5} (1 cm in the model corresponds to about 60–600 m in nature).

The silicone putty (SMG36 produced by Dow Corning) is used to simulate viscous layers such as salt or under-compacted shales layers in sedimentary basins. The silicone putty, under laboratory conditions, behaves as a Newtonian fluid (Weijermars, 1986) with a viscosity equal to 5.10^4 Pa s and a density of 0.97 g/cm^3. The silicone putty must satisfy the following similarity criterion:

$$\eta^* = \delta^* g^* \lambda^* \tau^* \qquad (3)$$

where η^*, δ^*, g^*, λ^*, and τ^* are the model-to-nature ratio for viscosity, density, gravity, length, and time, respectively. In our models, η^* is about 10^{-14}, δ^* is about 0.6, g^* is equal to 1, and λ^* is about 1.5×10^{-5}. Thus, to satisfy Eq. (3), τ^* is about 10^{-9} (1 h in the model represents about 100,000 years in nature).

Two parameters were varied: the presence of basal silicone putty and the velocity of extension. Two experiments were performed without silicone at two different velocities (0.023 and 0.05 mm/s), and three experiments were performed with basal silicone putty at three different velocities (0.011, 0.023 and 0.05 mm/s). The models are deformed at strain rates between 2×10^{-5} s^{-1} and 10^{-4} s^{-1}. The last value is similar to Ackermann et al. (2001). This lower velocity is used to explore the role of low silicone strength, as it is proportional to velocity (and viscosity):

$$R = h\eta\epsilon' \qquad (4)$$

where R, h, η, and ϵ' are the strength, the thickness, the viscosity and the strain rate of the silicone layer, respectively. The extension is transmitted from the base of the model and then is different from a far-field extension. Questions could also arise from the coupling between the rubber sheet and the silicone and between the silicone and the sand layer. These experimental conditions are discussed in a later section.

Finally, as illustrated in Section 3.1 and reported by recent works (Clifton et al., 2000; Ackermann et al., 2001), the modes of faulting in wet clay are close to natural brittle deformation. Thus, although the models might not be perfectly scaled, they are useful to simulate natural extensional features.

2.2. Data processing

2.2.1. Fault detection
The deformed models are analyzed using topographic information. A three-dimensional (3D) laser-beam scanner allows us to digitize the model topography (Fig. 4a) and build a digital elevation model in the central part of the experiment avoiding edge effects. The laser resolution is 0.25 mm in the x, y, z directions. From this topographic data, a slope map is calculated using a gradient matrix. Fault surfaces are extracted by fixing a threshold on the slope map (Fig. 4b). This map contains three values: (i) white for low slope area, (ii) blue for west, and (iii) red for east dipping faults. The last step consists of the automatic digitization of the fault polygons (Fig. 4c). As the fault polygons are extracted from the topographic map, each segment building these polygons is contained in a 0.25×0.25 mm cell. Finally, the fault polygons that crosscut the edge of the analyzed area are automatically removed from the fault list. The topographic map and the list of fault polygons contain the entire information about the 3D-fault surface (i.e. x, y, z coordinates, strike, dip direction, length, throw). These parameters are used to quickly compute scaling relationships such as the displacement–length relationship.

2.2.2. Displacement–length relationship
Below a throw of about 0.25 mm, fault length is underestimated and the trend of the dataset in this area has a lower slope than in the large length area (Fig. 5). For this reason, the throw length relationship is calculated in the area of medium to large throw and length (i.e. the data in the black continuous envelope in Fig. 5). The relationship is then calculated over one order of magnitude of length and throw.

For practical reasons, the throw–length relationship will be used in this paper as a proxy for the displacement–length relationship with the implicit assumption that all the faults have the same dip. Nonetheless, faults tend to rotate with increasing applied strain and their dip decreases from an initial value of 70° to about 55°. Long faults have generally a longer history than short faults, they have accumulated more displacement and rotation toward lower dip. Therefore, the throw–length plot underestimates the contribution of large faults with respect to a displacement–length plot. Quantitatively, the slope of the throw–length relationship in a log/log plot should be lower than the one that would have been measured on a log/log displacement/length plot. However, we keep the throw–length relationship as a proxy for the displacement–length relationship because we are not interested in the absolute value of the displacement–length slope and this bias mainly affects the very late stages of the experiments.

2.2.3. Deformation map and participation ratio
From the map of fault polygons and measured throw, 'deformation' maps can be computed to study the spatial

a) Topography

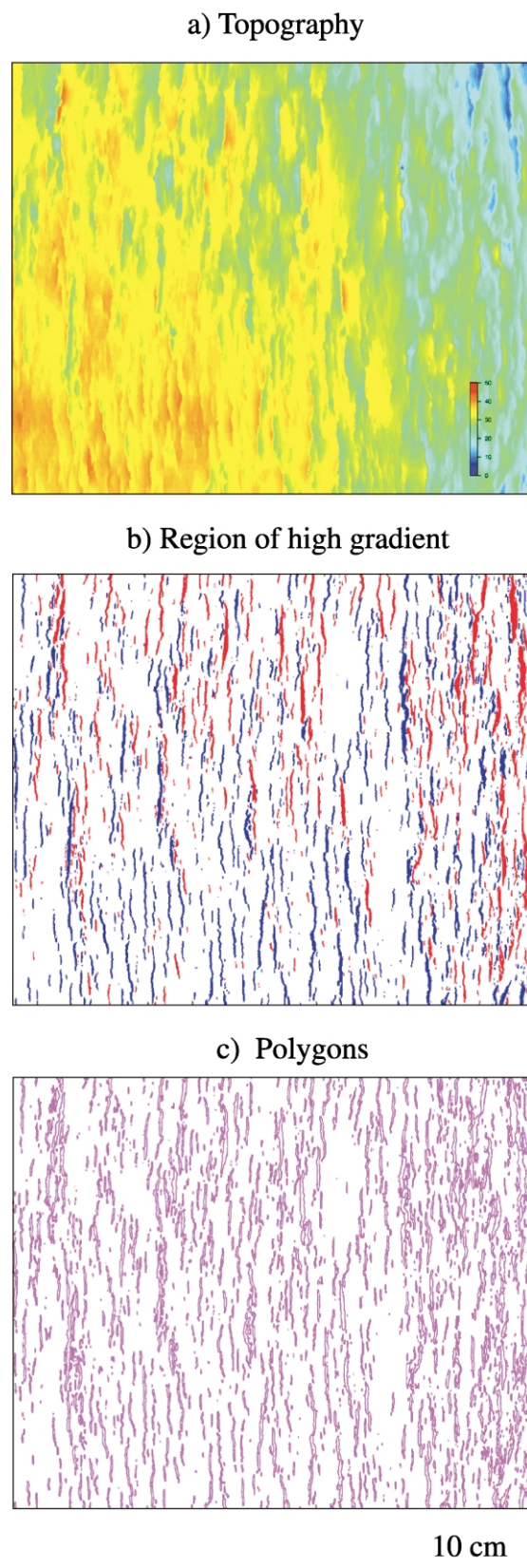## b) Region of high gradient

c) Polygons

10 cm

Fig. 4. Steps of the data processing. (a) Digital topography of the model. (b) Fault surfaces obtained from a gradient map and using a threshold on slopes (high gradients). (c) Map of the faults represented by their outline (polygons), which contains all the geometrical information (azimuth, length, throw and dip).
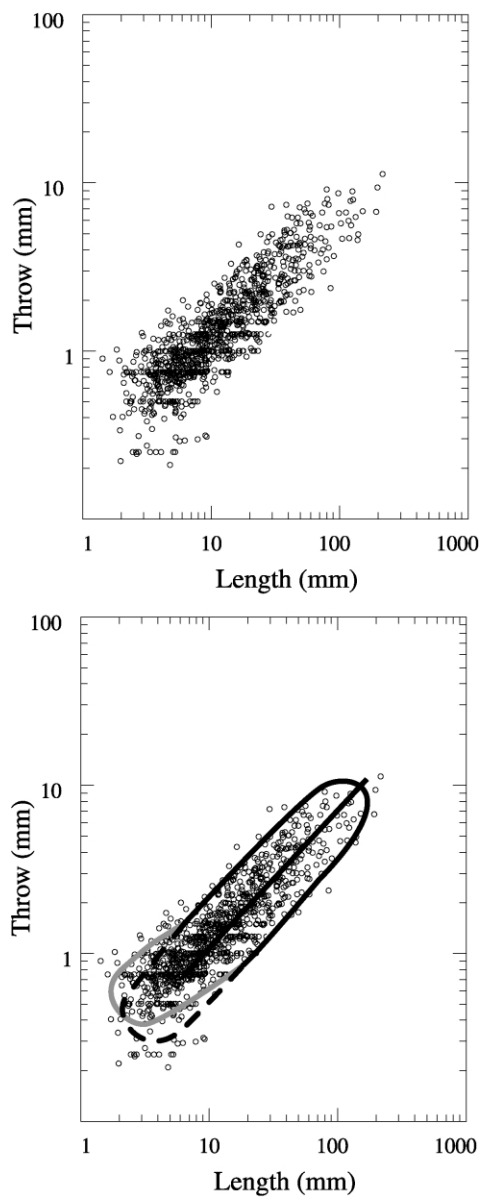

Fig. 5. Calculation of displacement–length relationship and effect of resolution. In log–log representation, the scatter of data is similar to the scatter of natural data. We see also the scatter linked to the resolution of the experimental system (multiples of 0.25 mm). The continuous envelope is the data envelope. The black one (continuous and dashed) is the envelope that we would have obtained without resolution problems: at small throws, the length is underestimated. The displacement–length relationship is computed only with the data in the continuous black envelope.

organization of deformation associated with faulting. A cell of these deformation maps can contain several fault segments. In each cell, we calculate the product of the length of each small segment of the faults (see Section 2.2.1) with the associated throw. The value d of each cell of the deformation map is then the sum of all these products. This measure is linearly related to strain, under the assumption that faults are dip-slip and have a more-or-less constant dip. Several deformation maps are computed changing the cell size. An increase of the cell size

corresponds to a resolution decrease. These deformation maps are then used to estimate the distribution of the deformation and its localization. The localization is the capacity of the deformation to be distributed heterogeneously in system (Davy et al., 1995). A participation ratio *P* is used to quantify the localization (Davy et al., 1995; Sornette et al., 1993). This ratio is defined as:

$$P = \frac{1}{S} \frac{(\sum d)^2}{\sum d^2} \qquad (5)$$

where *S* is the total number of pixels in the map, *d* the value of each cell of the deformation map (see above). *P* compares areas affected by deformation with the total area; a lower ratio indicates greater localization (Davy et al., 1995). *P* is computed for three experiments with basal silicone putty and two experiments without basal silicone putty, from deformation maps that have been computed with various resolutions (Fig. 6). When the resolution decreases (large size of cell), the participation ratio increases because a low resolution has the effect of diffusing the measure of the deformation. From Fig. 6, we see that two curves cross at certain resolutions. These crossings are artefacts caused by measurement inaccuracy. In this case, we consider the curves identical.

2.2.4. Measured extension versus applied extension

Due to the resolution dependency of *P*, a second quantitative method is used, where the ratio *E* between the measured extension and the applied extension is calculated. Heaves are summed along cross-sections in the extension direction and a ratio is calculated with these heave sums over the extension applied. This ratio *E* is plotted versus the extension applied (Fig. 7) for the five experiments. As
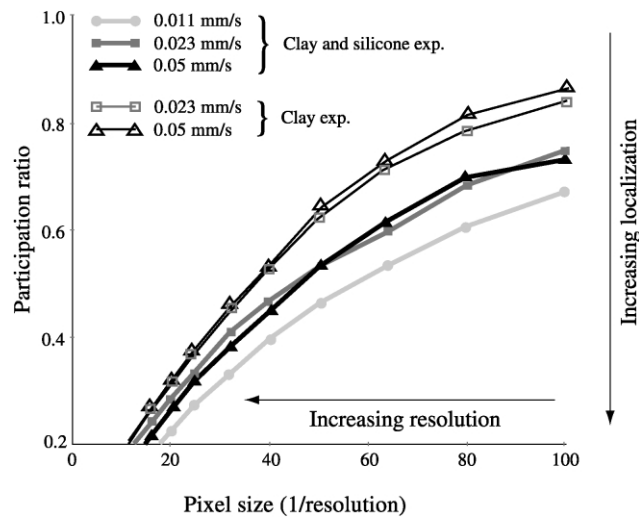
Fig. 6. Participation ratio *P* as a function of the resolution. This ratio is calculated for different sizes (0.25–100 mm) of pixel of the deformation map. A large pixel means a low resolution. The deformation is localized (low value of *P*) when this ratio is small. Here the ratio is smaller in the case of a low extension velocity. The deformation is then particularly localized with low strength silicone.
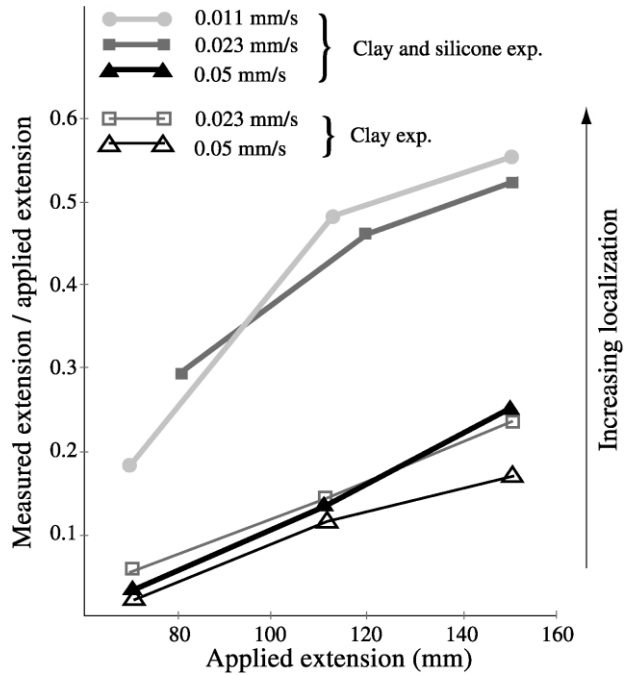
Fig. 7. Measured extension/applied extension ratio *E* as a function of the extension. This ratio is higher when the extension is accommodated by faults above the laser resolution. When the extension velocity is high, very small faults are numerous and *E* is low. When *E* is high, the extension is accommodated by large faults; the deformation is more localized, as in the low velocity case.

expected, this ratio is smaller than one because the applied extension is accommodated by continuous deformation of the wet clay layer (Ackermann et al., 2001) and by small faults not detected by the laser (throws below 0.25 mm). Thus, this ratio is an indicator of the relative importance that the deformation accommodated for small-scale features: a higher ratio indicates a larger contribution of the large faults on deformation. As explained above in the case of the participation ratio, some curves cross. These crossings are not significant and the crossing curves can be considered as identical.

3. Results

3.1. Fault network characteristics and scaling relationships

In the experiments, faults propagate by a combination of two mechanisms: (i) radial propagation (isolated growth by tip propagation) and (ii) segment linkage (Fig. 8). The radial propagation is the most important mechanism during the early stages of extension (Fig. 8a). Faults grow separately, their displacement and length are increasing simultaneously to produce quite symmetric throw profiles. Faults then start to interact when their length is sufficiently large to create overlap (Fig. 8b). In this case propagation is disturbed, throw profiles become asymmetric and throw increases faster than length. After this period of interaction, the two
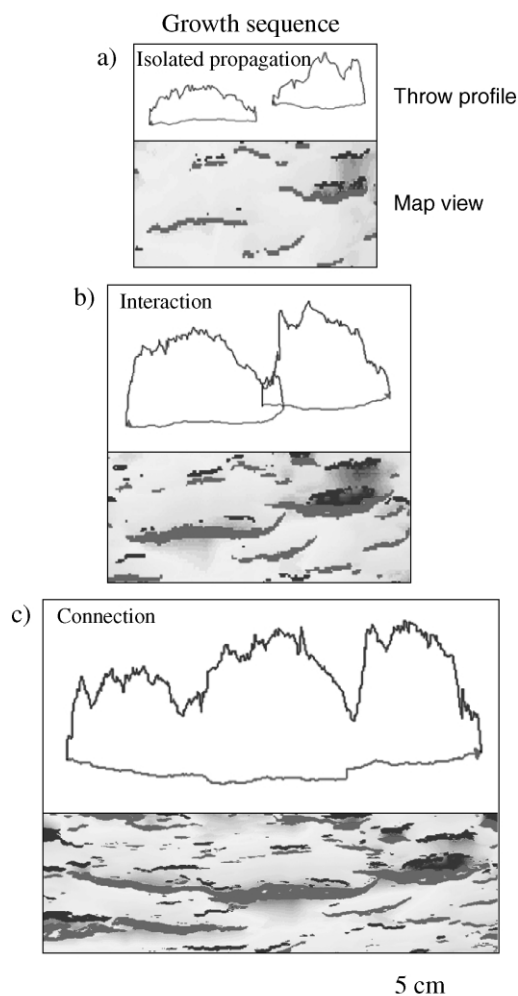
Growth sequence

Fig. 8. Growth sequence observed in the clay models. Topography map and throw profiles are shown. (a) Two faults grow by tip propagation. The maximum throw is about 4 mm. (b) The faults start to interact and a segment turns toward the other one. The maximum throw is about 7 mm. (c) Both the segments are connected and form a single fault (another is connected on the left of the map). At this last step, the maximum throw is 10 mm.

segments frequently link (Figs. 3 and 8c). Connections can also occur before the formation of a relay zone when the segments turn toward each other before propagating fault tips overlap (Fig. 3). The resulting fault shows typical undulations and an irregular throw profile (Fig. 8c). As already reported by Clifton et al. (2000) and Ackermann et al. (2001), the propagation sequence of faults in the wet clay is closely similar to the propagation sequence of natural faults.

Quantitatively, the maximum displacement (D)–length (L) relationship has been computed for three steps of extension of each experiment and is characterized by the relation expressed by Eq. (1). The scatter exhibited by the data (Fig. 5) has been frequently observed and explained by the mechanism of segment linkage both in natural fault networks (Cartwright et al., 1995) and other analogue models (Mansfield and Cartwright, 2001). The scatter at low

displacement values is also caused by the resolution of the laser beam (0.25 mm) and the related inaccuracy of throw and length measurements. The scaling exponent n of the different fault networks varies between 0.6 and 1 (Table 1). These values are consistent with those obtained by Ackermann et al. (2001) and in some natural cases (Fossen and Hesthammer, 1997; Gross et al., 1997; Ackermann and Schlische 1999).

3.2. Localization of deformation

Even though the effects of mechanical properties and thickness of a brittle layer on fault patterns are well known, the effects of a viscous layer underlying a brittle layer are still not well documented. Therefore, we compare the distribution of deformation on one-layer wet clay and two-layer wet clay/silicone models (Fig. 9). The first stages of extension (less than 7%) are difficult to analyze because the size of the faults is commonly below the resolution of the laser beam, and also because some extension may be accommodated by continuous deformation. Even though the networks are quite similar, the distribution of the deformation is clearly more heterogeneous and the maximum displacements are more important with a basal viscous layer. When extension values are larger than 15%, the evolution of the two fault networks is very different. Without the silicone layer, new faults initiate and grow continuously, resulting in a relatively homogeneous fault pattern. In contrast, in the presence of a basal silicone layer, few faults initiate and develop, accommodating the major part of the applied extension. This style of deformation produces non-deformed zones bounded by faults with large displacement. The participation ratio P (Fig. 6) quantifies the difference between clay and clay/silicone models. At a fixed resolution, the ratio P calculated for clay experiments is systematically higher than in clay/silicone experiments, whatever the velocity (see, for example $v = 0.023$ mm/s of the experiment displayed in Fig. 9). The ratio E of measured extension over applied extension (Fig. 7) allows us to study how the model accommodates the extension. Large ratios (close to one) indicate that large faults develop. Low ratios indicate that the extension is accommodated by smaller faults (and very small faults not well detected). The ratio E
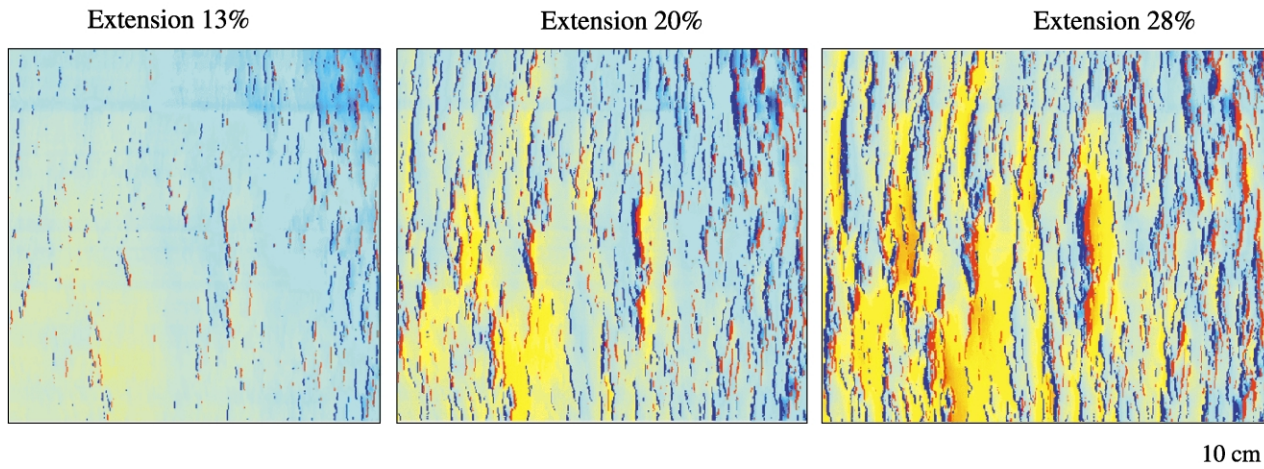
Table 1
List of scaling exponent of displacement–length relationship for each experiment. The three steps of extension are computed (Ext.: amount of extension). Sil.: two-layers experiments (sand and silicone putty). Three exponents are not given because regression was not satisfactory

	Ext. 13%	Ext. 20%	Ext. 28%
0.05 mm/s		0.59	0.68
0.023 mm/s		0.64	0.66
Sil. 0.05 mm/s		0.80	0.76
Sil. 0.023 mm/s	0.83	0.87	0.85
Sil. 0.011 mm/s	0.77	0.89	0.97

a) Clay and silicone, velocity 0.023mm/s

Extension 13%   Extension 20%   Extension 28%

10 cm

b) Clay, velocity 0.023mm/s

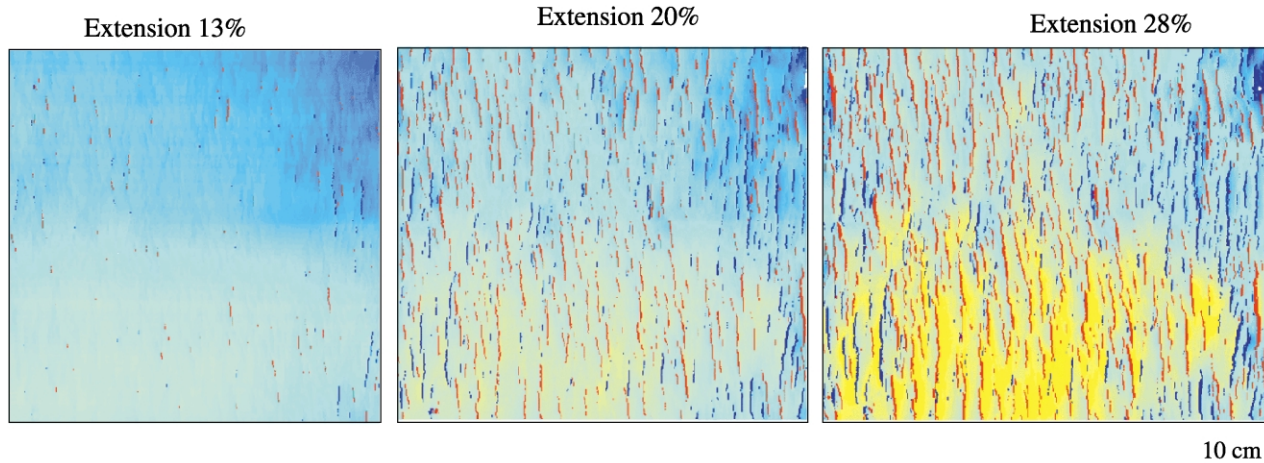Extension 13%   Extension 20%   Extension 28%

10 cm

Fig. 9. Comparison between fault networks generated in clay with and without basal silicone. In models with basal silicon, the spatial distribution of the faults is more heterogeneous and the displacements are larger. Large zones are not deformed; few small faults exist, except in the vicinity of large faults. In clay experiments, unfortunately, an initial topography gradient of a few millimetres is caused by the initial deposition of the wet clay. However, this gradient is perpendicular to the extension direction and tends to disappear with increasing extension. This gradient is then assumed not to influence the evolution of the experiments and not to alter the results.

for experiments with basal silicone layer is systematically higher than in experiments without basal silicone. Fault networks in clay/silicone models are composed of faults with a statistically larger displacement than in clay models. This observation, combined with qualitative comparison of network and results of participation ratio calculation, highlights that the deformation is more localized in models with a basal silicone layer.

In wet clay/silicone models, an important parameter is the extension velocity as it controls the strength of the viscous layer (Eq. (4)). Its effects on the fault network are studied comparing the networks generated in clay and silicone models with various velocities (Fig. 10). The experiments demonstrate that lower velocities result in larger fault throws with large undeformed zones. This mean that at low extension velocities or low silicone strength deformation is more localized. This is also demonstrated by

the participation ratio decrease at low velocity. At velocities of 0.05 and 0.023 mm/s, the curves are very close, while the curve for the velocity $v = 0.011$ mm/s is lower, illustrating the localization of the deformation. P is a normalized ratio that measures the spatial distribution of the deformation and not its intensity. Looking at the fault network, the spatial distribution of the deformation is similar in the experiments performed at 0.05 and 0.023 mm/s (Figs. 9 and 10). This explains why the two corresponding participation ratios are very close.

For the model with low extension velocity (0.011 mm/s), the ratio E (measured over applied extension) is large (Fig. 7). Most of the extension is accommodated by large faults, localizing the deformation. However, the curves for velocities $v = 0.011$ and 0.023 mm/s are very close compared with the curve of the 0.05 mm/s velocity experiment. The extension accommodated by large faults

Extension 20%   Extension 28%

Extension velocity
0.05mm/s

a)

10 cm

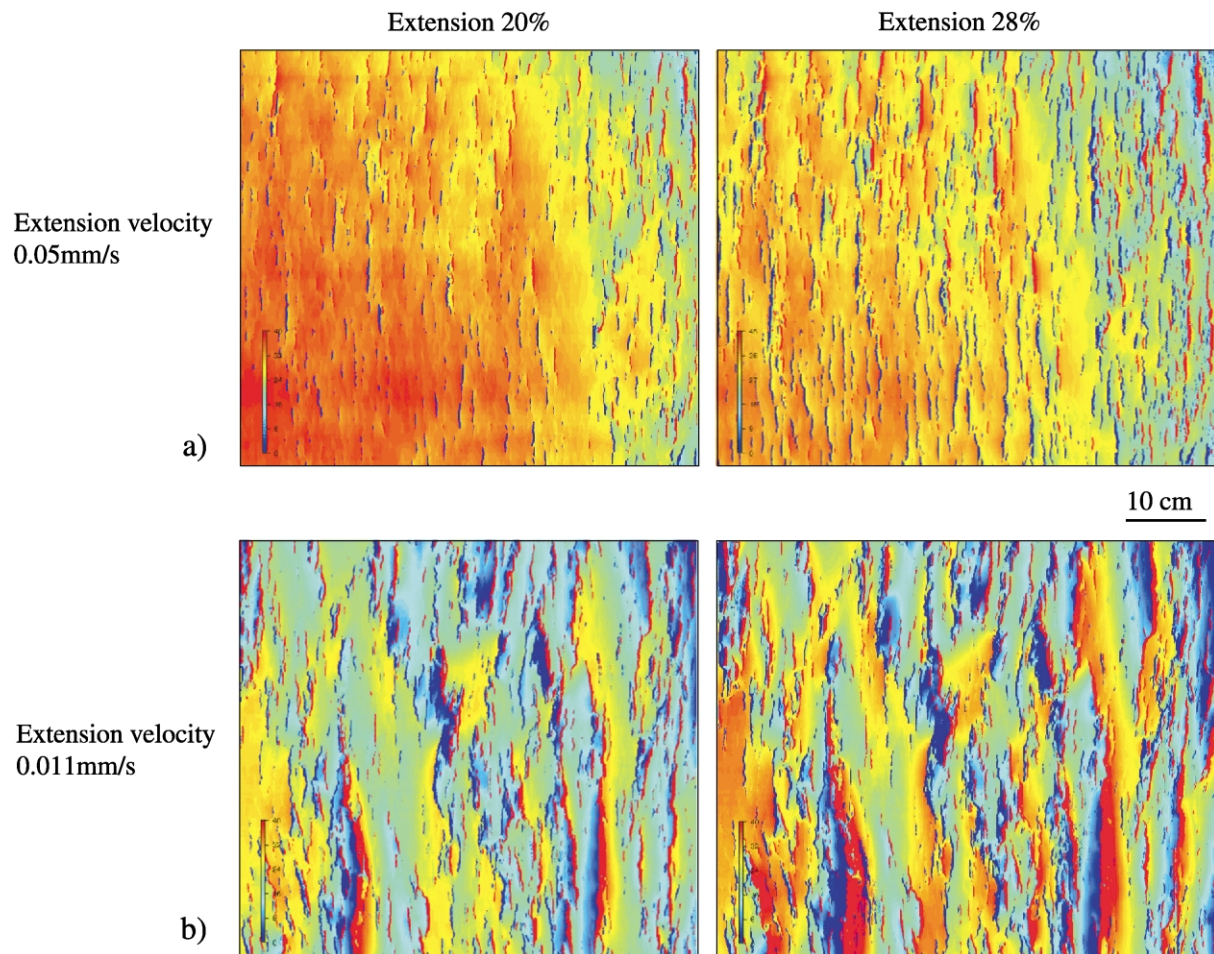Extension velocity
0.011mm/s

b)

Fig. 10. Comparison between fault networks generated in clay with basal silicon for two different extension velocities. The slower the velocity, the more heterogeneous and localized the spatial distribution of faults. A slow extension velocity enhances the effect of presence of basal silicone as shown in Fig. 9.

is effectively almost the same for the two experiments (0.011 and 0.023 mm/s). This result combined with that of the participation ratio provides interesting information. For fast extension velocity (i.e. 0.05 mm/s), the deformation is 'homogeneously' distributed. For lower extension velocity (i.e. 0.023 mm/s), the deformation is also 'homogeneously' distributed, but the extension is accommodated by larger faults. Finally, for the lowest extension velocity (i.e. 0.011 mm/s), the deformation is more heterogeneously distributed and the extension accommodated by large faults is similar to the one of the previous experiment. In summary, these experiments show that: (i) the presence of a basal viscous layer induces a localization of the deformation, and (ii) a low extension velocity, applied at the base of the model, enhanced this phenomenon.

3.3. Small faults

So far we have demonstrated that the characteristics of the viscous layer strongly influence the geometry of the fault pattern as a whole. This section demonstrates that its effect is also significant when describing the relationship between large and small faults.

Large faults generated in analogue models with strongly localized deformation accommodate most of the applied extension. In this case, the creation of new major faults is limited. Genetically there are essentially three kinds of small new faults (small length and throw) (Fig. 11); their number, position and orientation are now discussed.

(a) The first population is generated by the extension applied at the base or at the lateral boundary of the model. Their initiation is limited in the case of strong localization because when the silicone layer is weak, few new faults initiate between the large faults. As in Gupta and Scholz (2000), the initiation of small faults is inhibited with increasing extension. This is particularly true with a weak basal layer. Thus, the position and creation of these small faults are controlled by the strength of the basal silicone. The early small faults became larger ones as they coalesced (Ackermann and Schlische, 1997; Cowie, 1998).

(b) The second population, antithetic faults, is genetically related to the presence of large displacement on faults, and thus initiate only in the vicinity of these large faults. In our models, the rheology influences their
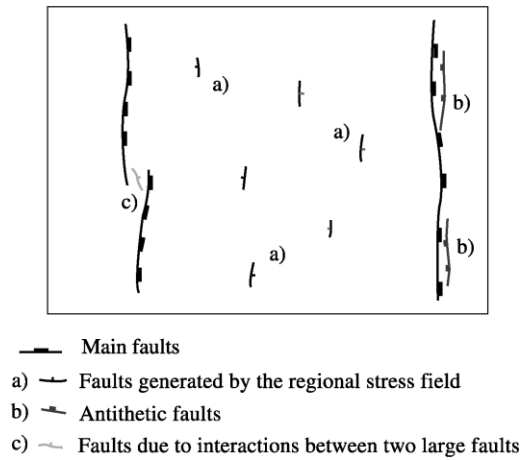
Fig. 11. The three main kinds of small new faults. (a) Faults generated by the regional stress field. (b) Faults due to large displacement accumulated on faults and block rotation. (c) Relay faults due to interactions between two larger faults.
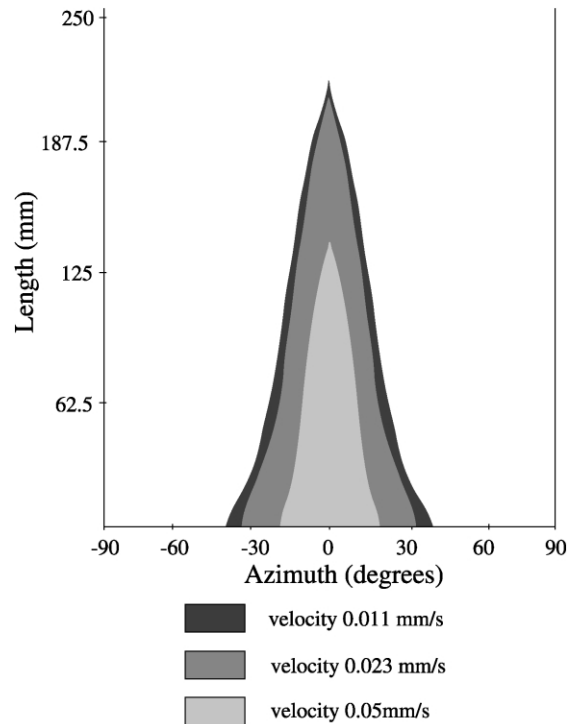

Fig. 12. Diagram of fault length as a function of orientation. The azimuth zero is perpendicular to the extension direction. The large faults are perpendicular to this extension direction, but the small have more dispersed orientations. This phenomenon is amplified by low silicone strength.

number as a weak silicone layer, producing large displacements, induces the creation of a large number of these faults. Meanwhile, their position and their orientation, which is parallel to the direction of the large faults, remain unchanged.

(c) The third population is generated in zones of interaction between two faults. This last kind of small faults is the population of faults created particularly in the case of relay ramp fracturing. The orientation of these faults is oblique to the average strike of the larger ones.

The measure of the dispersion of fault orientation (Fig. 12) gives two results. The first is a greater dispersion of small faults than larger ones. The activity of a large fault perturbs the stress field, in particular the directions of principal stresses around normal faults (Simon et al., 1999). Near the centre of the fault, stress releases occur, especially in the footwall block. At the fault tips, stress accumulations and perturbations (Kattenhorn et al., 2000) and interactions between faults (Crider and Pollard, 1998) perturb the stress field in relay zones. The orientation of principal stresses is then changed and new small faults initiate according to this local stress field. These perturbations should be enhanced by the accumulation of displacement on large faults. Thus, the phenomenon is amplified with the evolution of the system, as an increase of total extension applied induces an increase of the throws and lengths of faults. The second result of Fig. 12 shows the increase of this dispersion with the decrease of silicone strength. This effect is explained by the increase of localization at low silicone strength that contributes to create large faults and then increases the role of relay zones, stress field perturbations, and dispersion of small fault directions.

From what we have seen so far, the position of small faults was influenced by the strength of the basal silicone layer and small faults are clustered around large faults when

the basal layer is weak, as only small relay faults and antithetic faults are initiated. In other cases, as in Ackermann and Schlische (1997), small faults are anti-clustered around larger faults. This suggests that fault clustering must be approached as a function of the rheology.

3.4. Numerical models

To complete and verify the results, the same experiments have been performed in mechanical simulations using a 2D numerical code (Paravoz, explicit hybrid finite-difference/-finite element code) (Poliakov and Hermann, 1994). In this code, based on the well-tested solver of the FLAC algorithm (Cundall, 1989), shear bands can develop spontaneously and thus can be assimilated to non-predefined faults. In the numerical experiments, the mechanical properties and boundary conditions have been reproduced as close as possible to those used in our analogue models (Fig. 13).

The Paravoz code is a fully explicit time-marching large-strain Lagrangian algorithm that solves the full Newtonian equation of motion:

$$\rho \frac{\partial}{\partial t}\left(\frac{\partial \mathbf{u}}{\partial t}\right) - \mathrm{div}\boldsymbol{\sigma} - \rho\mathbf{g} = 0 \qquad (6)$$

coupled with constitutive equations of kind:

$$\frac{D\boldsymbol{\sigma}}{Dt} = F\left(\boldsymbol{\sigma}\left(\mathbf{u}, \nabla\frac{\partial \mathbf{u}}{\partial t}, ...T...\right)\right) \qquad (7)$$
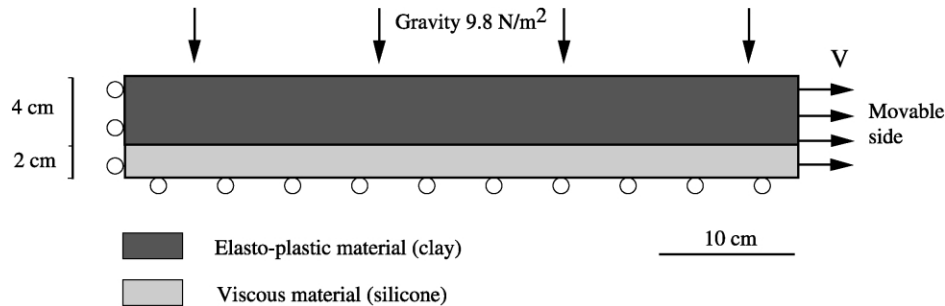
Fig. 13. Boundary conditions and mechanical properties of the numerical simulations. The conditions and mechanical properties are almost the same as in the analogue models. Elasto-plastic layer: the Lamé coefficients are equal to 0.02 MPa, the cohesion and the friction angle are 50 Pa and 30°, respectively. Viscous layer: the viscosity is 5.10^4 Pa s. The boundary conditions are identical except the bottom condition that, here, is a horizontal free-slip condition.

and with those of heat transfer (not used in our experiments). In these equations, **u**, **σ**, and **g** are the vector-matrix terms for the displacement, stress, and acceleration due to body forces, respectively. The terms t and ρ, respectively, designate the time and density. The terms $\partial/\partial t$, D/Dt, and F denote a time derivative, an objective time derivative and a functional of the variables given in brackets, respectively.

Solution of the equations of motion provides velocities at mesh points, which permit calculation of element strains. These strains are used in the constitutive relations to calculate element stresses and equivalent forces, which form the basic input for the next calculation cycle. To solve explicitly the governing equations, the FLAC method uses a dynamic relaxation technique by introducing artificial masses in the inertial system. This technique is capable of modelling physically highly unstable processes and of handling strongly non-linear rock rheologies in their explicit form of the constitutive relationship between strain and stress. The code handles plastic and viscous strain localization, which allows simulation of formation of non-predefined shear bands. The brittle properties of the wet clay were simulated using Mohr–Coulomb plasticity with friction angle of 30° and cohesion of 50 Pa. The values of the elastic Lamé constants were equal to 0.02 MPa. The silicone was simulated as a Maxwell fluid with effective viscosity of 5×10^4 Pa s (Newtonian viscous behaviour with an elastic component, which can be schematically illustrated by a serial connection of an elastic spring and a viscous dash pot damper).

The numerical grid was formed from 500×60 quadrilateral elements (respectively, horizontally and vertically) composed of 2000×240 triangular sub-elements (each quadrilateral element consists of four triangular elements, to minimize mesh locking (Cundall, 1989). The resulting numerical resolution was very high (four triangular elements per square millimetre, which approaches the resolution of the laser scanner used in the experimental models). The upper boundary was set as a free surface, a horizontal velocity V was imposed on the right boundary and the left boundary was fixed horizontally, with a free slip condition in the vertical direction (Fig. 13). At the bottom

boundary, a horizontal free-slip condition was used, whereas the vertical velocity was set to zero. No velocity field was applied at the bottom, in contrast to the analogue models where the shear with the underlying rubber sheet induced a velocity field that linearly increased from the fixed side to the moving one.

Two basic situations were tested using two different horizontal boundary velocities (0.011 and 0.05 mm/s). The cross-sections show the total plastic strain (Fig. 14) that develops through time and is expressed as synthetic and antithetic shear bands. At the beginning, single shear bands develop and secondary antithetic shear bands initiate, forming conjugate sets that merge generally close to the elasto-plastic/visco-elastic contact. In the first 8% of extension of the 0.05 mm/s experiment, approximately 10 shear bands initiate. After 20% of extension, the number of shear bands has doubled. All shear bands, the earlier ones and the later ones, continue to be active.

In the 0.011 mm/s experiment, the shear bands are less numerous and accommodate a large part of the applied deformation. They become very complex with the creation of new secondary shear bands, but no new deformed zone is created, and the plastic strain intensity in the shear bands is higher than in the 0.05 mm/s case. The deformation of the brittle layer is similar to boudinage, where some zones are intensively thinned while others are undeformed without significant rigid rotation. The comparison of these two simulations demonstrates remarkable similarity to the analogue models, where low extension velocity (i.e. low silicone strength) produces localization of the deformation.

4. Discussion

4.1. Experimental conditions

Before stating any conclusions, several experimental conditions need to be discussed: the behaviour of the wet clay, the coupling between the rubber sheet and the silicone layer and between the silicone layer and the brittle layer.

The behaviour of the wet clay is not perfectly established and is known to be partly viscous. Ackermann (1997)
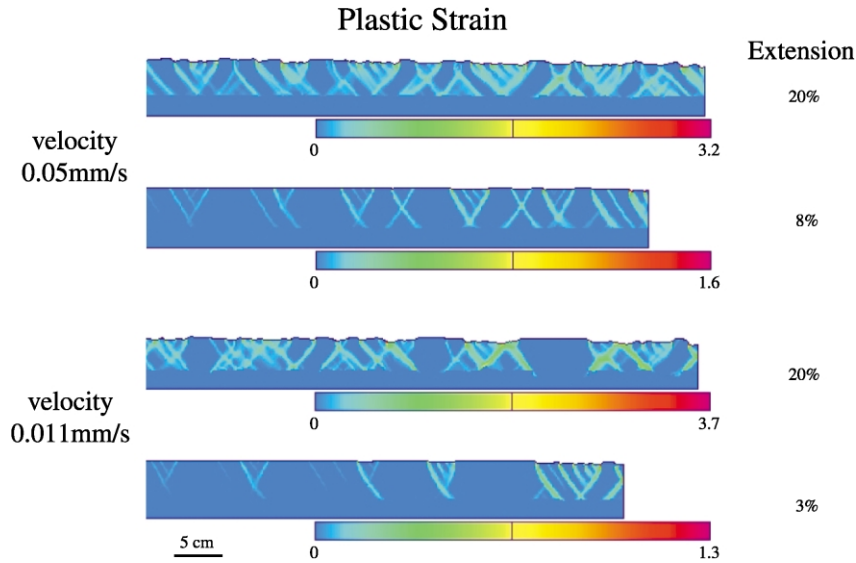
Plastic Strain

Fig. 14. Results of the numerical simulations. The total plastic strain (length variation over initial length) accumulated in the model is shown. The deformation is more localized when the velocity is low. In this case, the shear bands are less numerous but each accommodates more extension.

showed that in one-layer clay models, the velocity of extension has an effect on the fault network, in the sense that fast strain rate could generate localized models. In our models (Fig. 15), visual comparison between two networks generated at different velocities (0.023 and 0.05 mm/s) shows that the geometries of the fault networks are similar. In the same way, the values of P and E at velocities of 0.023 and 0.05 mm/s are close (Fig. 6). The small differences that we can observe are much smaller than the difference between the two experiments with silicone with corresponding velocities. The introduction of a basal viscous layer radically changes the deformation evolution. Thus, the velocity has a strong effect on the silicone layer strength (as expected) and this effect is much more important than the effect on the clay layer strength. This shows that the viscous behaviour of the wet clay can be neglected under the conditions of the experiments described here.

The question about coupling and boundary conditions can be approached through the numerical simulations. In these models, the extension is applied by moving a lateral vertical boundary and not through the base of the model. The phenomenon of localization highlighted in laboratory experiments should not be attributed to the basal conditions of extension, as we also observe this localization in numerical experiments.

Finally, in the numerical models, the interface between the brittle and the viscous layer is set as 'sticky'. The localization is not an artefact that is caused by problems of coupling along interfaces; the variation of extension velocity only influences the rheology of the models and would have the same effect as a variation of the viscosity of the silicone layer. These results thus confirm that the viscous layer strength controls the localization of the deformation in the brittle layer, as observed in the wet clay/silicone models.

a) Clay, velocity 0.05mm/s, extension 28%
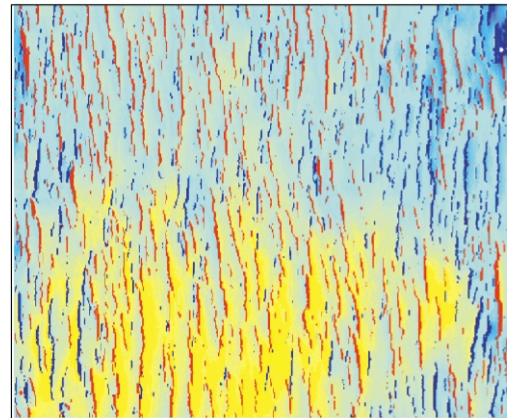
b) Clay, velocity 0.023mm/s, extension 28%
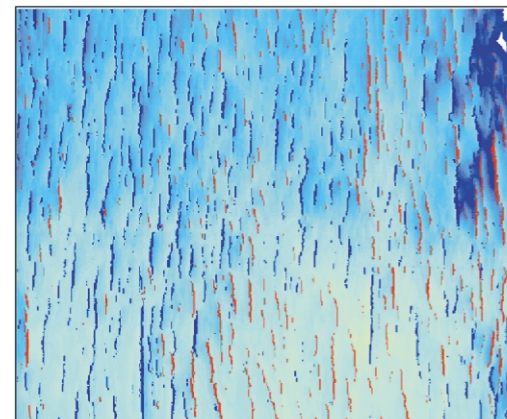
10 cm

Fig. 15. Comparison between fault networks generated in clay without basal silicone for two different extension velocities. The extension velocity slightly affects spatial distribution of faults.

4.2. Evolution of the displacement–length relationship

The evolution with time of the displacement–length relationship is poorly constrained. We here show that its scaling exponent varies as a function of both the rheology and the amount of extension.

We observe that the scaling exponent (slope of the regression line in log–log space) depends on the rheology of the model. The presence of weak silicone induces higher values of *n* (Table 1) that indicate a more localized deformation as the viscous basal layer favours the creation of high displacement with respect to lengths. Moreover, the range of displacement (between large and small faults) is higher than in delocalized models, which induces a higher displacement–length scaling exponent. Ackermann et al. (2001) showed that a thick brittle layer favours steeper slopes (high value of *n*) than thinner models. A decrease of silicone strength and increase of brittle thickness have similar results: a higher scaling exponent *n* and a localized deformation. In other words, in the presence of basal silicone, the brittle layer is stratigraphically unconfined (Schultz and Fossen 2002) and favours accumulation of displacement.

Furthermore, the rheology also controls the evolution with amount of extension of the scaling exponent. At high silicone strength (high velocity of extension), there is no evident evolution of *n* with increasing strain (Table 1). The scaling exponent seems to be more or less constant or to decrease. This last case would signify that length increases faster per unit of displacement and this result is consistent with Ackermann et al. (2001). Fault linkage and the associated increase of length explain this behaviour well.

However, at very low silicone strength (low extension velocity, 0.011 mm/s) the exponent increases with amount of extension (Table 1). In these localized models, the evolution suggests that displacements increase faster than length and shows that the presence of a weak silicone layer, favouring larger displacement, can change the time evolution of the scaling exponent. Such an increase was inferred in several works (Morewood and Roberts, 1999; Gupta and Scholz, 2000; Poulimenos, 2000), which showed that, in high strain settings, displacement is accommodated on faults that are no longer growing in length. This can be caused by lateral inhibition of tip propagation because of the perturbed stress around other faults (Contreras et al., 2000; Gupta and Scholz, 2000; Poulimenos, 2000). As explained in Section 2.2.2, the scaling exponent of the displacement–length relationship is underestimated in the last stages of extension because of fault rotation and decreasing fault dip. This underestimation supports our interpretation as we should have obtained higher exponents, at high amount of extension and low viscous layer strength.

A stratigraphic confinement (that increases with the strength of the basal layer) influences fault growth in the sense that they grow in length more rapidly than in displacement. When the brittle layer is unconfined (for example when a low strength viscous layer is present at its base as in this study) or when the lateral propagation is inhibited, the displacement can increase more rapidly and the scaling exponent of the displacement–length relationship is higher and increases with time.

4.3. Role of viscous layers at various scales

The localization of the deformation in our experiments occurs when the extension is accommodated along large faults and induces an increase of the displacement–length relation exponent. The localization of the deformation occurs because the weak viscous layer allows the blocks between main faults to sink in this viscous layer. Hence, large accumulations of displacement along the faults are possible. Then the faults that exist at a given time (or a given amount of extension) can accommodate most of the applied extension during an increment of deformation. No faults will initiate in the non-deformed regions, as the stresses are completely released by accumulation of displacement on the existing faults. Moreover, the low strength of the silicone allows this material to flow from the subsiding block toward the elevated block. This silicone flow tends to enhance the displacement along the faults as a feedback mechanism. When the lower layer has a high strength (strong viscous layer or another brittle layer), the faults must deform or break a harder material at the base of the brittle layer to accumulate further displacement. In this case, less energy is necessary to initiate new faults and to accommodate the increasing extension.

At the lithospheric scale, the lower crust is embedded between two brittle layers, the brittle crust and the brittle lithospheric mantle. Crustal extension might be controlled by failure in the brittle mantle and by the lower crust, which transmits stresses vertically but distributes them horizontally (Allemand and Brun, 1991). Different laboratory experiments (Allemand, 1988; Brun and Beslier, 1996; Brun, 1999; Michon and Merle, 2000) showed that the geometry of the deformation in the analogue upper crust is controlled by the rheology of the ductile lower crust. In these studies, low strain rates (i.e. low ductile strength) produce a localized deformation. This type of deformation is characterized by a narrow zone (single graben) or by tilted blocks separated by faults with large displacements. Such a deformation pattern is found in the Gulf of Suez, for example, where blocks between major faults are almost non-deformed (Colletta et al., 1988).

It is also noteworthy that natural rocks have strongly strain-rate dependent ductile rheology. For such rheology, the interaction between the brittle and ductile layers in asymmetric lateral boundary velocity settings (extension from one side) necessarily results in lateral variations in the effective viscosity of the lower ductile crustal layer. The faults forming in the vicinity of the moving boundary are characterized with higher slip and strain rates than those located at the stable side (e.g. middle of a rift basin).

Consequently, the brittle–ductile boundary at the moving side experiences faster vertical strains than that at its stable side. If the viscosity of the underlying ductile layer is stress and strain-rate dependent, we would infer additional reduction of the effective viscosity of the ductile layer in the vicinity of the moving side of the system. Though we are conscious of the importance of such behaviours, we choose to ignore them, as the strain-dependence behaviour of rocks is not yet well calibrated.

In other analogue and numerical models, deformation above reactivated basement faults is influenced by the presence of a viscous layer between the basement fault and the cover sequence (Schultz-Ela, 1994; Withjack and Callaway, 2000). Even though the basal conditions are different than in the present work, some similar conclusions are obtained.

In our experiments, under homogeneous basal boundary conditions, the deformation in the brittle layers can be localized in the presence of low strength viscous layers. These homogeneous basal conditions simulate the conditions at the upper crustal scale in a rifted continental area. In these tectonic environments, the conditions at the base of the brittle layers are difficult to establish. Is the extension transmitted from a deeper level in a homogeneous way or in a localized area (velocity discontinuity) or transmitted only by a far-field stress state? We have shown that in all these cases the presence of a weak basal viscous layer could produce localization of deformation, even under homogeneous basal conditions. Furthermore, the stress state could be intermediary between these different solutions. The basal condition may be between the two end-members: a homogeneous and a localized transmission.

5. Conclusions

This work is based on detailed analysis of wet clay/silicone experiments evolution in extension. In these experiments, the growth sequence of the normal faults is a combination of two mechanisms: the radial propagation and the connection of segments. The displacement–length relationship exhibits a power-law form. This study shows that:

(i) The presence of a basal viscous layer and its strength has a strong influence on the deformation pattern in the brittle layer. It produces a localization of the deformation, i.e. a heterogeneous distribution of faults. In this case, the deformation is accommodated by large faults in few areas while other areas are almost undeformed. This phenomenon is amplified by a low strength of the silicone. The localization of the deformation influences the small-scale faulting in terms of spatial organization and fault orientations (clustering their position in the vicinity of large faults and scattering their orientation). A characterization of the rheology of the deformed system is then very important when studying the evolution of a fault network.

(ii) The scaling exponent of the displacement–length relationship increases with the decrease of silicone strength. It is caused by a strong localization of the deformation. In this case large faults are very important and grow faster than smaller faults. An increase of the exponent is also found with increasing extension at low silicone strength, while a decrease of the exponent through time is found at high silicone strength. Because of this time- and rheology-dependence, it seems fruitless to search for universal statistical parameters describing natural fault networks. To validate the evolution through time of a scaling exponent, we have now to find direct links between this evolution and the growth sequence. In any case, an estimate of the amount of extension accommodated by the system is then necessary.

The understanding of the geometry of a complete fault network and the prediction of sub-seismic faults must therefore take into account both the rheology of the entire deformed system and the amount of extension.

Acknowledgements

References

Ackermann, R.V., 1997. Spatial distribution of rift related fractures: field observations, experimental modeling, and influence on drainage networks. Unpublished PhD thesis, Rutgers University.

Ackermann, R.V., Schlische, R.W., 1997. Anticlustering of small normal faults around larger normal faults. Geology 25, 1127–1130.

Ackermann, R.V., Schlische, R.W., 1999. Uh-Oh! $n < 1$: dynamic length–displacement scaling. Eos 80, S328.

Ackermann, R.V., Schlische, R.W., Withjack, M.O., 2001. The geometric and statistical evolution of normal fault systems: an experimental study of the effects of mechanical layer thickness on scaling laws. Journal of Structural Geology 23, 1803–1819.

Allemand, P., 1988. Approche expérimentale de la mécanique du rifting continental. Unpublished Ph.D. thesis, Université de Rennes I.

Allemand, P., Brun, J.P., 1991. Width of continental rifts and rheological layering of the lithosphere. Tectonophysics 188, 63–69.

Brun, J.P., 1999. Narrow rifts versus wide rifts: inferences of rifting from laboratory experiments. Philosophical Transaction of the Royal Society of London 357, 695–712.

Brun, J.P., Beslier, M.O., 1996. Mantle exhumation at passive continental margin. Earth and Planetary Science Letters 142, 161–173.

Buck, W.R., Lavier, L.L., Poliakov, A.N.B., 1999. How to make a rift wide. Philosophical Transaction of the Royal Society of London 357, 671–693.

Cartwright, J.A., Trudgill, B.D., Mansfield, C.S., 1995. Fault growth by segment linkage: an explanation for scatter in maximum displacement and trace length data from the Canyonlands Grabens of SE Utah. Journal of Structural Geology 17, 1319–1326.

Cartwright, J.A., Mansfield, C., Trudgill, B., 1996. The growth of normal faults by segment linkage. In: Buchanan, P.G., Nieuwland, D.A. (Eds.), Modern Developments in Structural Interpretation, Validation and Modelling. Geological Society of London Special Publication 99, pp. 163–177.

Clark, R.M., Cox, S.J.D., 1996. A modern regression approach to determining fault displacement–length scaling relationships. Journal of Structural Geology 18, 147–152.

Clifton, A.E., Schlische, R.W., Withjack, M.O., Ackermann, R.V., 2000. Influence of rift obliquity on fault-population systematics: results of experimental clay models. Journal of Structural Geology 22, 1491–1509.

Cloos, E., 1968. Experimental analysis of gulf coast fracture patterns. The American Association of Petroleum Geologists Bulletin 52, 420–444.

Colletta, B., Le Quellec, P., Letouzey, J., Moretti, I., 1988. Longitudinal evolution of the Suez rift structure (Egypt). Tectonophysics 153, 221–233.

Contreras, J., Anders, M.H., Scholz, C.H., 2000. Kinematics of normal fault growth and fault interaction in the central part of Lake Malawi Rift. Journal of Structural Geology 22, 159–168.

Cowie, P.A., 1998. A healing-reloading feedback control on the growth rate of seismogenic faults. Journal of Structural Geology 20, 1075–1087.

Cowie, P.A., Scholz, C.H., 1992a. Displacement–length scaling relationship for faults: data synthesis and discussion. Journal of Structural Geology 14, 1149–1156.

Cowie, P.A., Scholz, C.H., 1992b. Physical explanation for the displacement–length relationship of faults using a post-yield fracture mechanics model. Journal of Structural Geology 14, 1133–1148.

Cowie, P.A., Vanneste, C., Sornette, D., 1993. Statistical physics model for the spatio-temporal evolution of faults. Journal of Geophysical Research 98, 21809–21821.

Crider, J.G., Pollard, D.D., 1998. Fault linkage: three-dimensional mechanical interaction between échelon normal faults. Journal of Geophysical Research 103, 24373–24391.

Cundall, P.A., 1989. Numerical experiments on localization in frictional materials. Ingenieur-Archiv 59, 148–159.

Davy, P., Hansen, A., Bonnet, E., Zhang, S.Z., 1995. Localization and fault growth in layered brittle–ductile systems: implications for deformations of the continental lithosphere. Journal of Geophysical Research 100, 6281–6294.

Dawers, N.H., Anders, M.H., Scholz, C.H., 1993. Growth of normal faults: displacement–length scaling. Geology 21, 1107–1110.

Fossen, H., Hesthammer, J., 1997. Geometric analysis and scaling relations of deformation bands in porous sandstones. Journal of Structural Geology 19, 1479–1493.

Gillespie, P.A., Walsh, J.J., Watterson, J., 1992. Limitations of dimension and displacement data from single faults and the consequences for data analysis and interpretation. Journal of Structural Geology 14, 1157–1172.

Gross, M.R., Gutiérrez-Alonso, G., Bai, T., Wacker, M.A., Collinsworth, K.B., Behl, R.J., 1997. Influence of mechanical stratigraphy and kinematics on fault scaling relations. Journal of Structural Geology 19 (2), 171–183.

Gupta, S., Scholz, C.H., 2000. Brittle strain regime transition in the Afar depression: implications for fault growth and sea-floor spreading. Geology 28, 1087–1090.

Hubbert, M.K., 1937. Theory of scale models as applied to the study of geologic structures. Geological Society of America Bulletin 48, 1459–1520.

Kattenhorn, S.A., Aydin, A., Pollard, D.D., 2000. Joints at high angles to normal fault strike: an explanation using 3-D numerical models of fault-perturbed stress fields. Journal of Structural Geology 22, 1–23.

Lavier, L.L., Buck, W.R., Poliakov, A.N.B., 1999. Self-consistent rolling-hinge model for the evolution of large-offset low-angle normal faults. Geology 27, 1127–1130.

Mansfield, C., Cartwright, J., 2001. Fault growth by linkage: observations and implications from analogue models. Journal of Structural Geology 23, 745–763.

Marchal, D., Guiraud, M., Rives, T., Van den Driessche, J., 1998. Space and time propagation processes of normal faults. In: Jones, G., Fisher, Q.J., Knipe, R.J. (Eds.), Faulting, Fault Sealing and Fluid Flow in Hydrocarbon Reservoirs. Geological Society of London Special Publication 147, pp. 51–70.

Marrett, R., Allmendinger, R.W., 1991. Estimates of strain due to brittle faulting: sampling of fault populations. Journal of Structural Geology 13, 735–738.

Michon, L., Merle, O., 2000. Crustal structures of the Rhine graben and the Massif Central grabens: an experimental approach. Tectonics 19, 896–904.

Morewood, N.C., Roberts, G.P., 1999. Lateral propagation of the surface trace of the South Alkyonides normal fault segment, central Greece: its impact on models of fault growth and displacement–length relationships. Journal of Structural Geology 21, 635–652.

Nicol, A., Walsch, J.J., Watterson, J., Gillespie, P.A., 1996. Fault size distributions—are they really power-law? Journal of Structural Geology 18, 191–197.

Peacock, D.C.P., Sanderson, D.J., 1991. Displacements, segment linkage and relay ramps in normal fault zones. Journal of Structural Geology 13, 721–733.

Pickering, G., Peacock, D.C.P., Sanderson, D.J., Bull, J.M., 1997. Modeling tip zones to predict the throw and length characteristics of faults. AAPG Bulletin 81, 82–99.

Poliakov, A.N.B., Hermann, H.J., 1994. Self-organized criticality in plastic shear bands. Geophysical Research letter 21, 2143–2146.

Poulimenos, G., 2000. Scaling properties of normal fault populations in the western Corinth Graben, Greece: implications for fault growth in large strain settings. Journal of Structural Geology 22, 307–322.

Schlische, R.W., Young, S.S., Ackermann, R.V., Gupta, A., 1996. Geometry and scaling relations of a population of very small rift-related normal faults. Geology 24, 683–686.

Scholz, C.H., Dawers, N.H., Yu, J.Z., Anders, M.H., Cowie, P.A., 1993. Fault growth and fault scaling laws: preliminary results. Journal of Geophysical Research 98, 21951–21961.

Schultz, R.A., Fossen, H., 2002. Displacement–length scaling in three dimensions: the importance of aspect ratio and application to deformation bands. Journal of Structural Geology 24, 1389–1411.

Schultz-Ela, D.D., 1994. Overburden structures related to extensional faulting beneath an intervening viscous layer. EOS, Transactions, American Geophysical Union Fall Meeting 75, 678.

Segal, P., Pollard, D.D., 1980. Mechanics of discontinuous faults. Journal of Geophysical Research 85, 4337–4350.

Simon, J.L., Arlegui, L.E., Liesa, C.L., Maestro, A., 1999. Stress perturbations registered by jointing near strike-slip, normal, and reverse faults: examples from the Ebro Basin, Spain. Journal of Geophysical Research 104, 15141–15153.

Sims, D., 1993. The rheology of clay: a modelling material for geologic structures. EOS, Transactions, American Geophysical Union Fall Meeting 74, 569.

Sornette, A., Davy, P., Sornette, D., 1993. Fault growth in brittle–ductile experiments and the mechanics of continental collisions. Journal of Geophysical Research 98, 12111–12139.

Vendeville, B., Cobbold, P.R., Davy, P., Brun, J.P., Choukroune, P., 1987. Physical models of extensional tectonics at various scales. In: Coward, M.P., Dewey, J.F., Hancock, P.L. (Eds.), Continental Extensional

Tectonics. Geological Society of London Special Publication 28, pp. 95–107.

Walsh, J.J., Watterson, J., 1988. Analysis of the relationship between displacements and dimensions of faults. Journal of Structural Geology 10, 239–247.

Watterson, J., 1986. Fault dimensions, displacements and growth. Pure and Applied Geophysics 124, 365–373.

Weijermars, R., 1986. Flow behavior and physical chemistry of bouncing putties and related polymers in view of tectonic laboratory applications. Tectonophysics 124, 325–328.

Withjack, M.O., Callaway, S., 2000. Active normal faulting beneath a salt layer: an experimental study of deformation patterns in the cover sequence. AAPG Bulletin 84, 627–651.

Withjack, M.O., Jamison, W.R., 1986. Deformation produced by oblique rifting. Tectonophysics 126, 99–124.

Yielding, G., Needham, T., Jones, H., 1996. Sampling of fault populations using sub-surface data: a review. Journal of Structural Geology 18, 135–146.